Runout error correction in tomographic reconstruction by intensity summation method

Ik-Hwan Kwon,[a] Jun Lim[b]* and Chung-Ki Hong[a]

[a]Department of Physics, POSTECH, 77 Cheongam-Ro, Nam-Gu, Pohang, Gyeongbuk 37673, Republic of Korea, and [b]Beamline Division, Pohang Light Source, 127 Jigok-Ro, Nam-Gu, Pohang, Gyeongbuk 37673, Republic of Korea. *Correspondence e-mail: limjun@postech.ac.kr

An alignment method for correction of the axial and radial runout errors of the rotation stage in X-ray phase-contrast computed tomography has been developed. Only intensity information was used, without extra hardware or complicated calculation. Notably, the method, as demonstrated herein, can utilize the halo artifact to determine displacement.

1. Introduction

Phase-contrast microscopy utilizes the artificial phase delay between the undiffracted reference wave and the diffracted object wave (Zernike, 1955). It is widely employed not only in optical microscopy but also in synchrotron hard X-ray microscopy image systems (Yin *et al.*, 2006). In synchrotron phase-contrast microscopy, the role of the rotation stage is to record successive transmission images necessary for a tomographic image dataset. The dataset is utilized by the back-propagation algorithm to reconstruct cross-sectional slice images of a specimen. This process is known as X-ray phase-contrast computed tomography (XPCT). Because XPCT is a non-destructive method for investigation of a specimen's structural information, it is used in various research fields such as material science, molecular and biochemical analysis, and others (Sakdinawat & Attwood, 2010; Stampanoni *et al.*, 2010; Mayo *et al.*, 2012). Recently, nanoscale-resolution X-ray absorption computed tomography combined with X-ray absorption near-edge spectroscopy (XANES) has been successfully applied in the battery research field (Meirer *et al.*, 2011; Wang *et al.*, 2014). In order to obtain more accurate chemical-mapping images of multi-particle battery materials, enhancement of three-dimensional resolution is most essential. The spatial resolution of a three-dimensional XPCT image is highly dependent on rotational-motion errors (axial runout error, radial runout error and wobble) incurred in the rotation stage (Parkinson *et al.*, 2012). Such errors are compensated for by measuring their displacements directly using capacitive sensors (Wang *et al.*, 2012; Xu *et al.*, 2014). Capacitive sensors, though requiring extra-high-precision hardware, can measure displacement to sub-50 nm. As an alternative means of error correction and alignment, feature tracking of fiducial markers (IMOD and SPIDER) has been developed (Dai *et al.*, 2013; Larabell & Le Gros, 2004). More recently, a method of feature-tracking alignment without fiducial markers has also been presented (Cheng *et al.*, 2014). In this study we focused on undesirable artifacts, known as halos, that normally appear in phase-contrast microscopy. Halos occur also in XPCT, because the phase retarder located
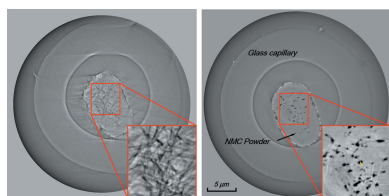
in the back focal plane of an objective lens also transmits a small degree of diffracted object wave (Yin *et al.*, 2012; Vartiainen *et al.*, 2014). Halos result in spurious bright areas around the phase sample or reverse contrast in images. In fact, in the line profile across a sample, there is a noticeably steep intensity gradient. In this paper we present an image alignment method that utilizes halos to measure axial and radial runout errors incurred in the rotation stage.

2. Experimental system

The 7C X-ray Nano Imaging (XNI) beamline at Pohang Light Source II is utilized for the purposes of hard X-ray phase-contrast microscopy. It applies off-axis illumination and a hole-type phase plate (Lim *et al.*, 2014) that offers the advantages of simple alignment, easy manufacture and significantly diminished halo-artifact effects. In particular, it provides high-contrast imaging of various bio-samples such as live cells, plants and human hair, among others. Normally, a two-dimensional image offers 46 nm resolution within a 40 µm field of view. In this study, as a specimen, we used micro-scale NMC (Ni/Mn/Co) cathode material powder attached to a 5 µm-thick thin-glass capillary by electrostatic force. The thin-glass capillary was pulled by a commercial puller (Narishige PC-10). The capillary was mounted on a three-axis piezo-driven scanning stage on top of an air-bearing rotation stage (Aerotech: model ABRS-150MP). The specifications of the rotation stage were as follows: <450 nm radial error motion; <175 nm axial error motion; <10 µrad wobble error. As an imaging objective, we used a 40 nm outermost-zone-width zone plate. The images were captured by a scintillator, 20× objective, and CCD (Apogee Imaging Systems; model U16MF) with 4096×4096 pixels of size 9 µm. The total magnification was 1285; the effective pixel size, correspondingly, was 7 nm. We obtained the tomographic image dataset by acquiring 361 equiangular projections between 0 and 180°.

3. Intensity summation method

The runout error of the rotation stage is readily defined by the boundary-position movement of a specimen. If we assume that the wobble error is negligible, the vertical width of the specimen in a successive tomographic image set is constant. Therefore, the axial runout error can be determined by measurement of the specimen's top position. However, the specimen cannot be used for radial runout error measurement, because its horizontal width alters according to the rotation angle. If we employ a cylindrical capillary parallel to the rotation stage, its width in the tomographic image set is constant regardless of the rotation angle. Thus, when the axis of the capillary is initially aligned with the axis of the rotation stage, one of its horizontal boundary positions can be used to determine the radial runout error. Typical X-ray images might include noise originating from the specimen (*i.e.* capillary, in the present case) holder. Such noise can incur serious error if a line profile is employed to determine the peak position. To solve this problem and also to increase the signal-to-noise
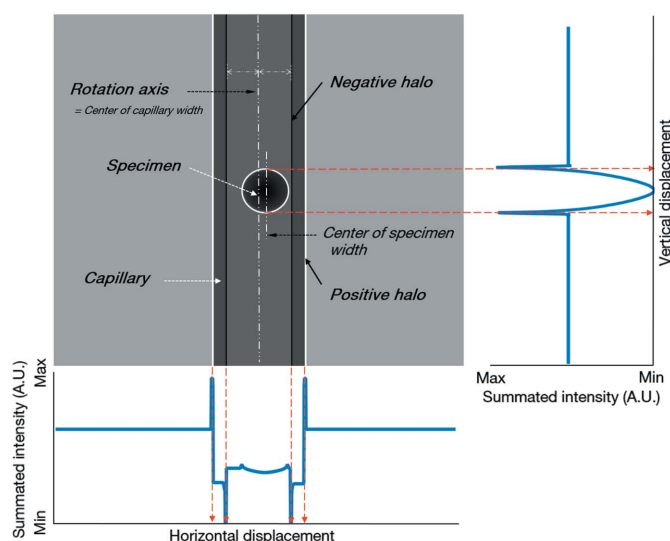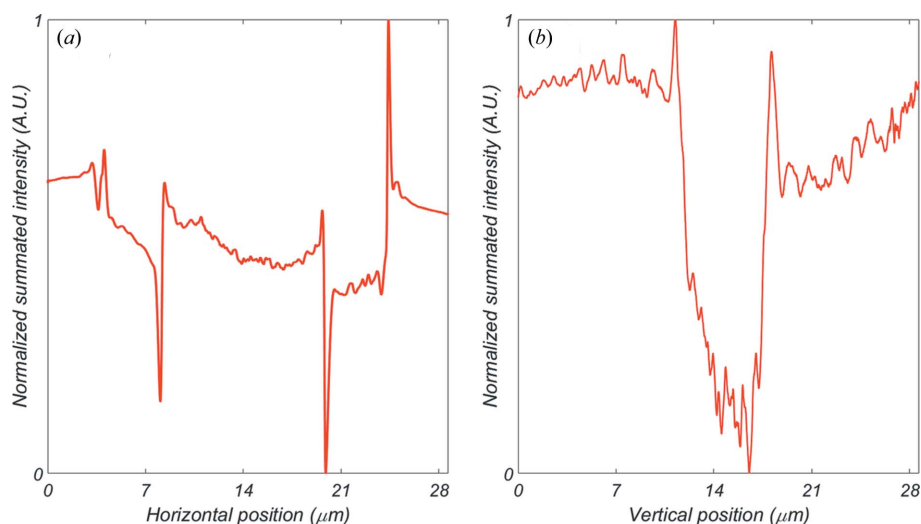

Figure 1
Virtual image of X-ray phase-contrast microscopy with summated intensity graph.

ratio, we used the intensity summation method. Fig. 1 shows an artificially transmitted X-ray image. First of all, in order to determine the specimen's top position, we summed the pixel intensities along each of the rows and plotted the information on the vertical axis. As expected, the intensity contribution due to the capillary was uniform in all of the rows. The halos shown at the top and bottom of the specimen caused the dominant high intensity. Inside the specimen by contrast, due to absorption, the intensity was relatively low. Next, in order to determine the boundary position of the capillary, we likewise summed the pixel intensities along each of the columns and plotted the results on the horizontal axis. The data show clearly that the halos at the capillary rims caused the maximum intensity. We then determined the peak intensity positions of the specimen and capillary. The movement of the top (or bottom) position of the specimen and the left (or right) boundary position of the capillary corresponded to the axial
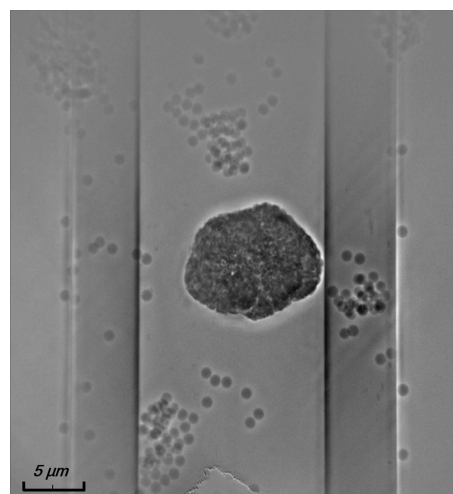
Figure 2
Projection image of specimen and capillary. The scattered spheres are 1.0 µm-diameter silicas.
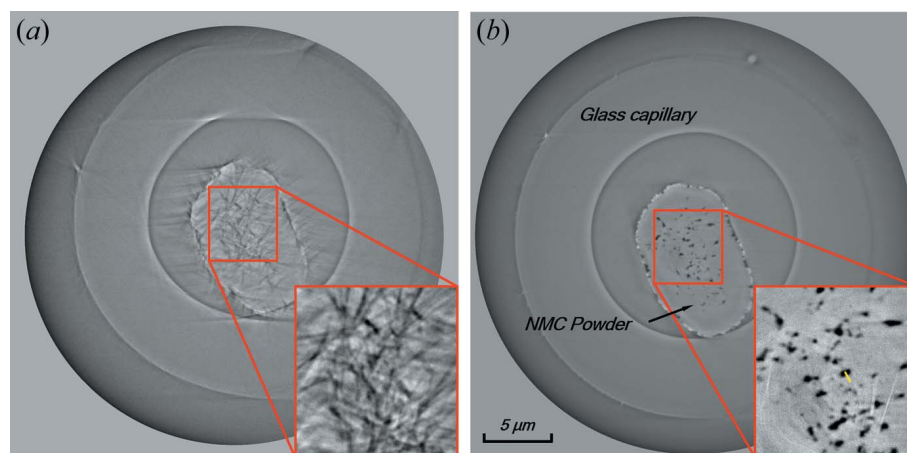
Figure 3
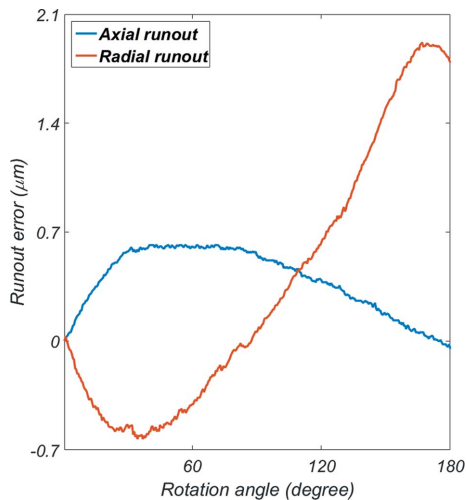Normalized summated intensities of the (a) horizontal and (b) vertical lines of Fig. 2.
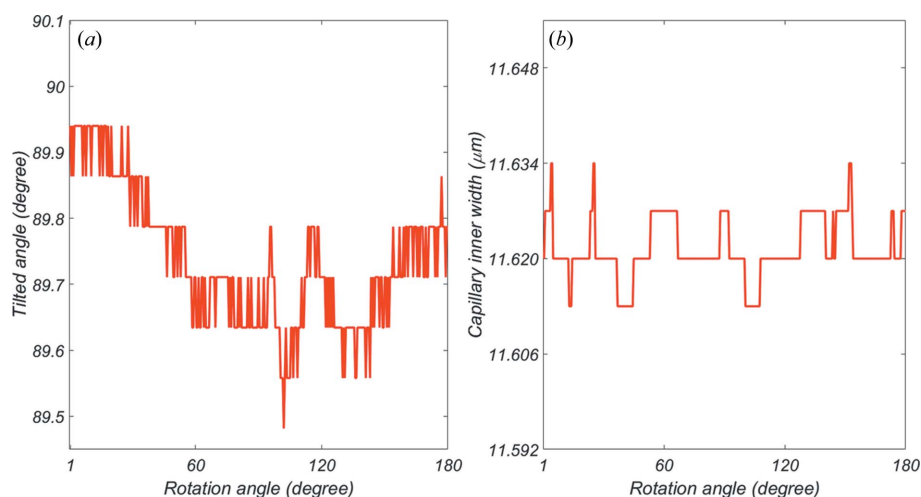
Figure 4
(a) Tilted angle of the capillary axis away from the vertical axis and (b) variation of inner width of the capillary.

measurement, we manually measured it over every rotation angle (Fig. 4a). The maximum variation was ∼0.5°, indicating that the error was less than 1 nm in the measurement of the specimen's top position, because the specimen turns in the vicinity of the rotation axis. This was negligible compared with the axial runout error. For this reason, even though we could not measure the tilt angle along the beam direction, we could assume that it was also negligible. Further, in order to determine the capillary's shape, we manually measured the inner width (Fig. 4b). As shown in the figure, the maximum variation of the width was ∼28 nm, which is considerable. We therefore cross-checked the reconstructed slice images. In this study we cannot remove the error due to the imperfectness but it should be corrected for resolution enhancement. After all, we are positioning the capillary vertically and then aligning all of the successive tomographic images to the initial state of the rotation axis and the top position of the specimen, finding that the rotation-stage runout errors were completely removed. Fig. 5(b) shows a post-alignment reconstructed slice image. Compared with the non-aligned image (Fig. 5a), the shape of the specimen and the capillary are clearly visible. The maximum radial motion error was determined to be ∼1.93 µm and the axial motion error ∼0.62 µm (Fig. 6). These results are much worse than the rotation-stage specifications would

and radial runout errors, respectively. Fig. 2 shows one of the projection images of the specimen and capillary. As can be seen, there were many 1.0 µm silica spheres that were attached in order to check the image contrast and resolution. Fig. 3 plots the summed intensities of the (a) horizontal and (b) vertical lines of Fig. 2. The result is rather different from the ideal case of Fig. 1, due to the non-uniform background and silicas. Also, the halos at the capillary rim are non-symmetric, due to the slight misalignment of the hole-type phase plate. In order to determine how the tilt angle of the capillary axis effected the axial runout error

Figure 5
Reconstructed slice images of NMC powder: (a) before and (b) after correction.

Figure 6
Axial and radial runout error of the rotation stage.

indicate. This might have been due to the cables of the three-axis piezo stage on the rotation stage. Next, the spatial resolution of the reconstructed slice image was evaluated separately by power spectrum analysis (Fig. 7a) and the knife-edge method (Fig. 7b). The results were 67 and 71 nm, respectively, quite consistent within the measurement error. The difference between the two-dimensional and three-dimensional resolutions, $\sim$20 nm, was due primarily to the imperfectness of the capillary width and rather small amount of image dataset. In summary, we could conclude that the cylindrical specimens were reconstructed almost perfectly without fiducial markers. On this basis, moreover, we proved that the capillary is a versatile tool for the purposes of secure sample holding and alignment in XPCT.
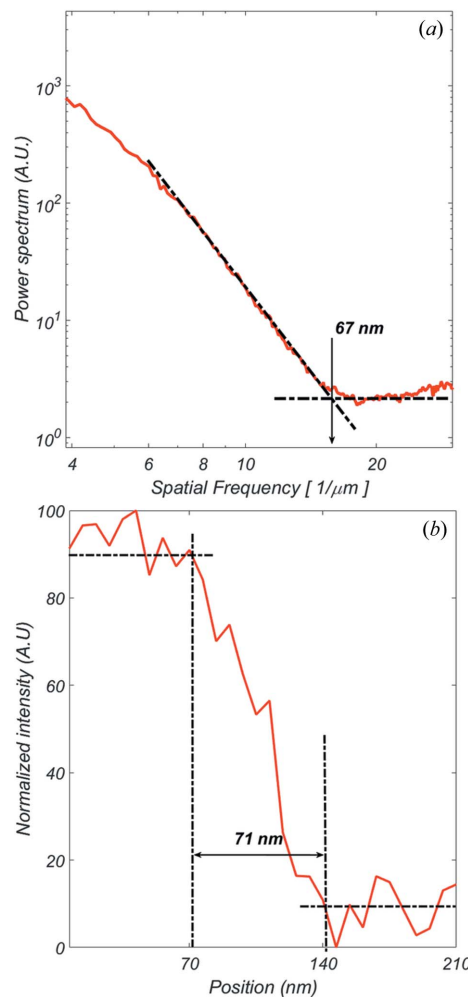
4. Conclusion

We have developed an alignment method to correct the axial and radial runout errors of the rotation stage in XPCT. This method is based only on intensity information; it entails no complicated calculations. We herein propose how to use the halo artifact for alignment. In the near future we will devise a method for imperfectness of capillary correction and spatial-resolution enhancement. Also, we are planning to construct a website that provides capillary-based alignment for the general user.

Acknowledgements

Figure 7
(a) Power spectra and (b) knife-edge intensity (yellow line) of the reconstructed slice image shown in Fig. 5(b).

References

Cheng, C. C., Chien, C. C., Chen, H. H., Hwu, Y. & Ching, Y. T. (2014). *PLoS One*, **9**, e84676.
Dai, W., Fu, C., Raytcheva, D., Flanagan, J., Khant, H. A., Liu, X., Rochat, R. H., Haase-Pettingell, C., Piret, J., Ludtke, S. J., Nagayama, K., Schmid, M. F., King, J. A. & Chiu, W. (2013). *Nature (London)*, **502**, 707–710.
Larabell, C. A. & Le Gros, M. A. (2004). *Mol. Biol. Cell*, **15**, 957–962.
Lim, J., Kim, H. & Park, S. Y. (2014). *J. Synchrotron Rad.* **21**, 827–831.
Mayo, S. C., Stevenson, A. W. & Wilkins, S. W. (2012). *Materials*, **5**, 937–965.
Meirer, F., Cabana, J., Liu, Y., Mehta, A., Andrews, J. C. & Pianetta, P. (2011). *J. Synchrotron Rad.* **18**, 773–781.
Parkinson, D. Y., Knoechel, C., Yang, C., Larabell, C. A. & Le Gros, M. A. (2012). *J. Struct. Biol.* **177**, 259–266.
Sakdinawat, A. & Attwood, D. (2010). *Nat. Photon.* **4**, 840–848.
Stampanoni, M., Mokso, R., Marone, F., Vila-Comamala, J., Gorelick, S., Trtik, P., Jefimovs, K. & David, C. (2010). *Phys. Rev. B*, **81**, 140105.
Vartiainen, I., Mokso, R., Stampanoni, M. & David, C. (2014). *Opt. Lett.* **39**, 1601–1604.
Wang, J., Chen-Wiegart, Y. & Wang, J. (2014). *Nat. Commun.* **5**, 4570.
Wang, J., Karen Chen, Y., Yuan, Q., Tkachuk, A., Erdonmez, C., Hornberger, B. & Feser, M. (2012). *Appl. Phys. Lett.* **100**, 143107.
Xu, W., Lauer, K., Chu, Y. & Nazaretski, E. (2014). *J. Synchrotron Rad.* **21**, 1367–1369.
Yin, G. C., Song, Y. F., Tang, M. T., Chen, F. R., Liang, K. S., Duewer, F. W., Feser, M., Yun, W. & Shieh, H. D. (2006). *Appl. Phys. Lett.* **89**, 221122.
Yin, Z., Kanade, T. & Chen, M. (2012). *Med. Image Anal.* **16**, 1047–1062.
Zernike, F. (1955). *Science*, **121**, 345–349.